

---

# Observation of the spin Nernst effect

**S. Meyer<sup>1,2</sup>, Y.-T. Chen<sup>3,4</sup>, S. Wimmer<sup>5</sup>, M. Althammer<sup>1</sup>, S. Geprägs<sup>1</sup>, H. Huebl<sup>1,2,6</sup>, D. Ködderitzsch<sup>5</sup>, H. Ebert<sup>5</sup>, G.E.W. Bauer<sup>3,7,8</sup>, R. Gross<sup>1,2,6</sup> and S.T.B. Goennenwein<sup>1,2,6</sup>**

1. *Walther-Meißner-Institut, Bayerische Akademie der Wissenschaften, Walther-Meißner-Straße 8, 85748 Garching, Germany*
2. *Physik-Department, Technische Universität München, 85748 Garching, Germany*
3. *Kavli Institute of NanoScience, Delft University of Technology, Lorentzweg 1, 2628 CJ Delft, The Netherlands*
4. *RIKEN Center for Emergent Matter Science (CEMS), 2-1 Hirosawa, Wako, Saitama 351-0198, Japan*
5. *Department Chemie, Physikalische Chemie, Universität München, Butenandtstraße 5-13, 81377 München, Germany*
6. *Nanosystems Initiative Munich (NIM), Schellingstraße 4, 80799 München, Germany*
7. *Institute for Materials Research, Tohoku University, Sendai, Miyagi 980-8577, Japan*
8. *WPI Advanced Institute for Materials Research, Tohoku University, Sendai 980-8577, Japan*

---

June 24, 2022

The observation of the spin Hall effect [1, 2] triggered intense research on pure spin current transport [3]. With the spin Hall effect [1, 4, 5], the spin Seebeck effect [6, 7, 8], and the spin Peltier effect [9, 10] already observed, our picture of pure spin current transport is almost complete. The only missing piece is the spin Nernst (-Ettingshausen) effect, that so far has only been discussed on theoretical grounds [11, 12, 13, 14]. Here, we report the observation of the spin Nernst effect. By applying a longitudinal temperature gradient, we generate a pure transverse spin current in a Pt thin film. For readout, we exploit the magnetization-orientation-dependent spin transfer to an adjacent Yttrium Iron Garnet layer, converting the spin Nernst current in Pt into a controlled change of the longitudinal thermopower voltage. Our experiments show that the spin Nernst and the spin Hall effect in Pt are of comparable magnitude, but differ in sign, as corroborated by first-principles calculations.

## 1 Main letter

Transverse transport is a key aspect of charge and/or spin motion in the solid state. In the charge channel, the Hall effect [15] and the Nernst effect [16] sketched in Fig. 1 (a), (b) enshrine transverse charge motion due to a gradient in the longitudinal potential imposed by an electric viz. thermal stimulus. Since the magnitude of the Hall charge current  $\mathbf{j}_c^{\text{Hall}} \propto \theta_H \mathbf{j}_c \times \mathbf{H}$  (parameterized by the Hall angle  $\theta_H$ , the applied charge current  $\mathbf{j}_c$  and the external magnetic field  $\mathbf{H}$ ) is governed by the density of mobile charge carriers in simple metals and semiconductors, Hall effect experiments quickly became a standard tool for material characterization. As sketched in Fig. 1(b), the transverse Nernst charge current  $\mathbf{j}_c^{\text{Nernst}} \propto \theta_N \nabla T \times \mathbf{H}$  is driven by a temperature gradient  $\nabla T$  or the corresponding heat current  $\mathbf{j}_h = -\kappa \nabla T$ , where  $\kappa$  is the thermal conductivity and  $\theta_N$  the Nernst angle.

Recently, electrically driven transverse *spin* transport in the form of the spin Hall effect (SHE) [17, 18] resulted in a new paradigm for spin-electronic device design [2, 19, 3]. The SHE refers to a transverse pure spin current  $\mathbf{j}_s^{\text{SH}} \propto \theta_{\text{SH}} \mathbf{j}_c \times \mathbf{s}$  driven by a charge current density  $\mathbf{j}_c$ , see Fig. 1(c). The spin Hall angle  $\theta_{\text{SH}}$  characterizes the charge-to-spin conversion efficiency [3, 20]. We here use the notation  $\mathbf{j}_s$  for the spin current density, while  $\mathbf{s}$  refers its spin polarization. In analogy to the Nernst effect, the spin Nernst effect (SNE) describes a transverse pure spin current  $\mathbf{j}_s^{\text{SN}} \propto \theta_{\text{SN}} \mathbf{j}_h \times \mathbf{s}$  arising from a longitudinal temperature gradient, cf. Fig. 1(d). Here,  $\theta_{\text{SN}}$  is the spin Nernst angle [11, 12, 13, 14]. In

spite of its fundamental importance for the understanding of pure spin current transport, up to now the SNE has remained a theoretical conjecture.

In this Letter, we report direct experimental evidence for the spin Nernst effect in platinum. In order to quantify the spin Nernst spin current, we modulate the transverse spin current transport boundary conditions and detect the spin accumulation induced by the spin Nernst effect (SNE) in the charge channel, via the inverse spin Hall effect (ISHE)[5]. In model calculations, we show that the combined action of SNE and ISHE results in a thermopower along the applied temperature gradient. This spin Nernst magneto-thermopower (SNMTP) is present in any electrical conductor with spin orbit coupling, but usually cannot be discerned from the conventional Seebeck effect, since it has the same symmetry. Only by selectively changing the spin transport boundary conditions, the SNMTP can be quantitatively extracted and analyzed.

The concept is illustrated in Fig. 2(a-d). A paramagnetic metal film is exposed to a temperature gradient  $\nabla T \parallel -\mathbf{x}$ . Through the Seebeck effect, a thermopower arises along  $\mathbf{x}$ . Furthermore, because of the SNE, a transverse spin current  $\mathbf{j}_s^{\text{SN}}$  is flowing along  $\mathbf{z}$  with spin polarization along  $\mathbf{y}$ , resulting in a spin accumulation at the metal film boundaries, as sketched in Fig. 2(a). The ensuing spin accumulation in turn drives a diffusive spin current  $\mathbf{j}_s^{\text{b}}$ . In the steady state, the spin current back flow  $\mathbf{j}_s^{\text{b}} = -\mathbf{j}_s^{\text{SN}}$  exactly balances the spin Nernst current, such that the net transverse spin current flow vanishes. Through the ISHE, both  $\mathbf{j}_s^{\text{b}}$  and  $\mathbf{j}_s^{\text{SN}}$  are accompanied by inverse spin Hall charge currents (cf. Fig. 2(b)). Since the latter are of equal magnitude but opposite in sign, they cancel. In that case the charge current vanishes and thereby the SNMTP. In contrast, when the transverse spin transport is short-circuited, the spins can not accumulate at the interface [Fig. 2(c)], such that  $\mathbf{j}_s^{\text{b}}$  is suppressed. As a consequence, only  $\mathbf{j}_s^{\text{SN}}$  drives an ISHE charge current that leads to a net charge current  $\mathbf{j}_c^{\text{ISHE,SN}}$  along  $\mathbf{x}$ , i.e., along the direction of the thermal bias [cf. Fig. 2(d)]. The combination of spin Nernst and inverse spin Hall effects thereby induces a thermopower along the temperature gradient with a magnitude depending on the transverse spin current boundary conditions. This SNMTP has the same symmetry as the conventional Seebeck effect, but nevertheless can be separated by modulating the transverse spin current boundary conditions by the spin transfer torque (STT) at the ferromagnetic insulator/normal metal (FMI/N) interface [21, 22]. The STT depends on the orientation of the magnetization  $\mathbf{M}$  in the magnetic insulator. If  $\mathbf{s}$  and  $\mathbf{M}$  are collinear (either parallel or antiparallel), the STT vanishes. This situation corresponds to open transverse spin transport boundary conditions [cf. Fig. 2(e)]. In contrast, if  $\mathbf{s}$  and  $\mathbf{M}$  enclose a finite angle, the STT is finite, becoming maximal for  $\mathbf{s}$  orthogonal to  $\mathbf{M}$  [short-circuit boundary conditions, Fig. 2(f)]. In our experiment, we control the transverse spin current boundary

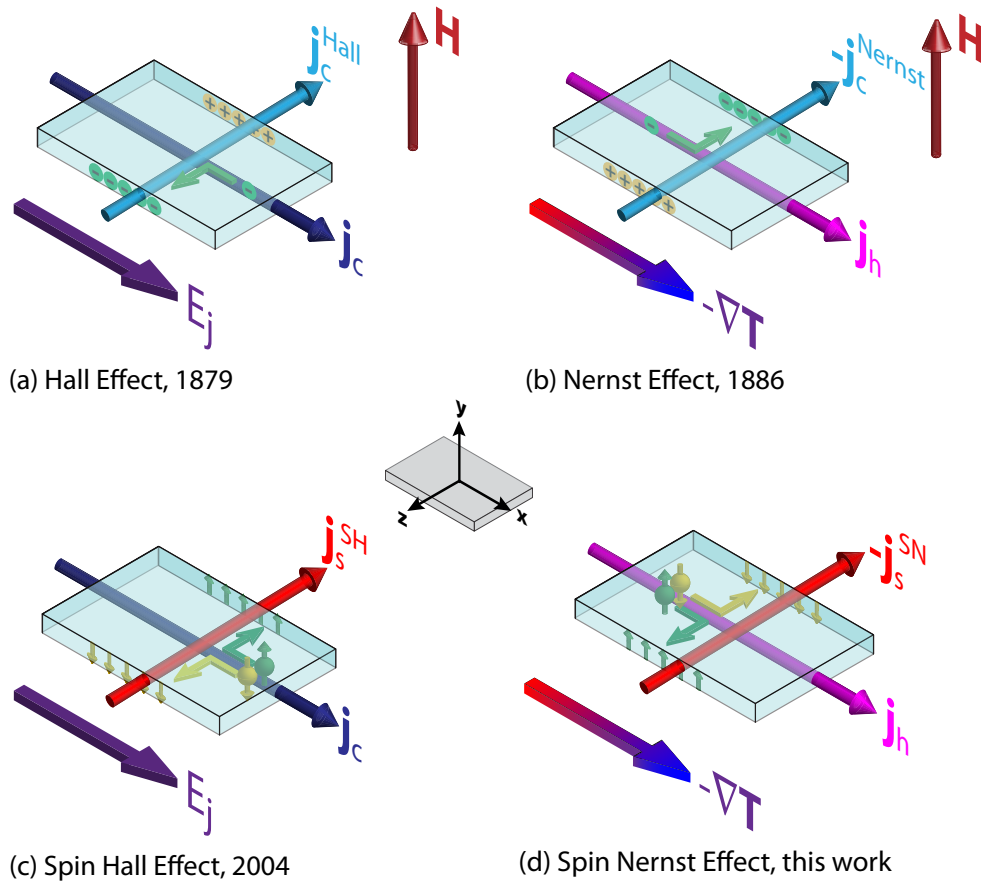


**Figure 1: Charge and spin-related electric and thermal effects.** (a) In the Hall effect, a transverse charge current density  $\mathbf{j}_c^{\text{Hall}}$  arises when a magnetic field  $\mathbf{H}$  and a charge current density  $\mathbf{j}_c$  are applied normal to each other. (b) The Nernst effect is the thermal analogue of the Hall effect. The electric effects are shown for negative charge carriers (electrons), translating into negative Hall and Nernst angles. (c) In the spin Hall effect, a transverse spin current density  $\mathbf{j}_s^{\text{SH}}$  perpendicular to the charge current density  $\mathbf{j}_c$  is generated due to spin orbit coupling. (d) A transverse spin current density  $\mathbf{j}_s^{\text{SN}}$  is also generated by a longitudinal temperature gradient. This effect has been named spin Nernst effect and is experimentally demonstrated here. The spin effects are shown for negative spin Hall and spin Nernst angles.

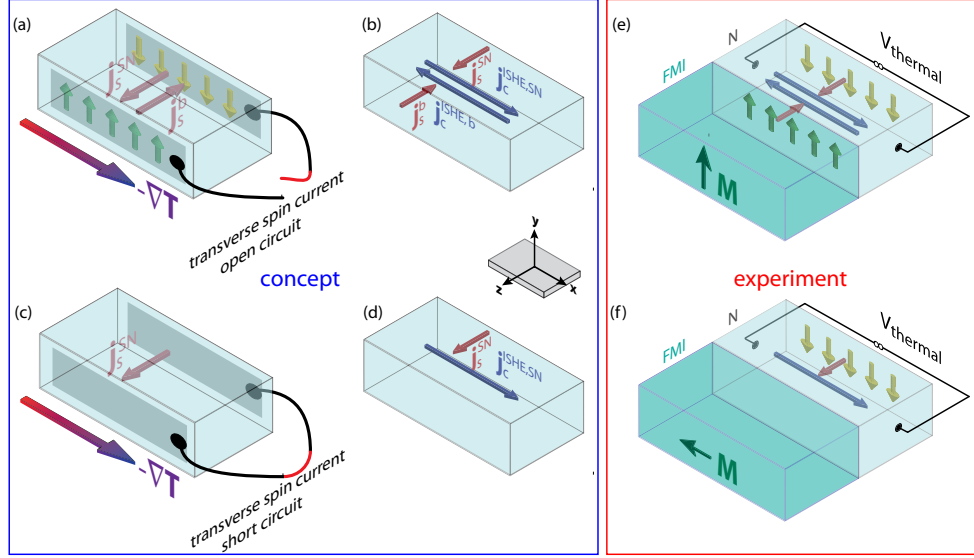


**Figure 2: Boundary conditions for the spin Nernst magneto-thermopower (SNMTP):** (a): A temperature gradient  $\nabla T$  along  $-\mathbf{x}$  evokes a spin current density  $\mathbf{j}_s^{\text{SN}}$  along  $\mathbf{z}$ , leading to a spin-dependent chemical potential along  $\mathbf{z}$ . Open circuit boundary conditions depicted in (a) block the transverse spin current, generating a spin current back flow  $\mathbf{j}_s^{\text{b}} = -\mathbf{j}_s^{\text{SN}}$ . (b) Both spin current densities  $\mathbf{j}_s^{\text{SN}}$  and  $\mathbf{j}_s^{\text{b}}$  give rise to charge current densities  $\mathbf{j}_c^{\text{ISHE,SN}}$  and  $\mathbf{j}_c^{\text{ISHE,b}}$  parallel and antiparallel to  $\mathbf{x}$ . (c) Short-circuiting the spin transport along  $\mathbf{z}$  suppresses the spin-dependent chemical potential and  $\mathbf{j}_s^{\text{back}}$ . (d) The absence of  $\mathbf{j}_s^{\text{back}}$  enhances the net charge current. (e,f) We utilize an insulating ferrimagnet (FMI) attached to the metal layer (N) to switch between open (no spin transfer torque, panel (e)) and short-circuit (finite spin transfer torque, panel (f)) boundary conditions by the FMI magnetization orientation  $\mathbf{M}$ .

conditions by systematically changing the orientation of the magnetization in the FMI layer, and record the ensuing spin Nernst driven changes in the thermopower, i.e., the SNMTP. The phenomenology of the SNMTP is similar to the recently established spin Hall magnetoresistance (SMR) [23, 24].

For a modeling of the SNMTP, we take into account the spin diffusion and dissipation in the metal, as detailed in the supplementary information. The thermopower  $V_{\text{thermal}}$  can be expressed in terms of an effective Seebeck coefficient as:

$$\frac{V_{\text{thermal}}}{l} = -[S + \Delta S_0 + \Delta S_1(1 - m_y^2)]\partial_x T \quad (1)$$

with

$$\frac{\Delta S_1}{S} = -\theta_{\text{SN}}\theta_{\text{SH}}\frac{\lambda}{t_{\text{N}}}\text{Re}\frac{2\lambda G \tanh^2(\frac{t_{\text{N}}}{2\lambda})}{\sigma + 2\lambda G \coth(\frac{t_{\text{N}}}{\lambda})}. \quad (2)$$

Here,  $t_{\text{N}}$ ,  $\sigma$  and  $\lambda$  are the thickness, electrical conductivity, and spin diffusion length of the N film, respectively,  $G$  the spin mixing conductance of the FMI/N interface,  $l$  the sample length and  $m_y = \mathbf{M} \cdot \mathbf{y}/|\mathbf{M}|$ . The sample is a Yttrium Iron Garnet ( $\text{Y}_3\text{Fe}_5\text{O}_{12}$ , YIG)|Pt bilayer [25] patterned into a Hall bar as shown in Fig. 3(a). An additional YIG|Pt strip extending in  $\mathbf{y}$  direction serves as an on-chip heater (OCH). We heat one side of the sample by applying a constant electric power of 286 mW to the OCH and connect the other end of the sample to a heat sink. This generates a temperature difference  $\Delta T = T_{\text{hot}} - T_{\text{cold}} = 18.0$  K between the two ends of the Hall bar as measured by on-chip resistive thermometry (see supplementary information for more details).

The external magnetic field of  $\mu_0 H = 1$  T applied to the sample is much larger than the demagnetization and anisotropy fields of YIG, such that  $\mathbf{M} \parallel \mathbf{H}$ . Then,  $\mathbf{H} \parallel \mathbf{y}$  corresponds to  $\mathbf{M} \parallel \mathbf{s}$  and thus open boundary conditions (no spin current flow across the interface), while for  $\mathbf{H} \parallel \mathbf{x}$  and  $\mathbf{H} \parallel \mathbf{z}$  the ferrimagnet represents an efficient spin current sink resulting in maximum spin current flow across the interface. The thermopower  $V_{\text{thermal}} = (\tilde{S} + \Delta S_1)\Delta T$  measured along the Hall bar direction  $\mathbf{x}$  [cf. Fig. 3(b)] contains the conventional Seebeck effect of the Pt Hall bar with the Seebeck coefficient  $\tilde{S}$  (for details see SI). For Pt,  $\tilde{S} < 0$ , such that the corresponding thermopower is negative. By rotating  $\mathbf{H}$  and therefore the magnetization  $\mathbf{M}$  of the YIG within the film plane from  $\alpha = 0^\circ$  ( $\mathbf{H} \parallel \mathbf{x}$ ) to  $\alpha = 90^\circ$  ( $\mathbf{H} \parallel \mathbf{y}$ ), the spin current boundary conditions are switched from short-circuit (finite transverse spin current) to open circuit (vanishing transverse spin current) conditions. The thermopower therefore shows a characteristic modulation as expressed by Eq. (1).

Our measurements confirm this expectation: For open boundary conditions,  $V_{\text{thermal}} = -66.225 \mu\text{V}$  is about  $\Delta V_{\text{thermal}} = 100$  nV larger than for short-

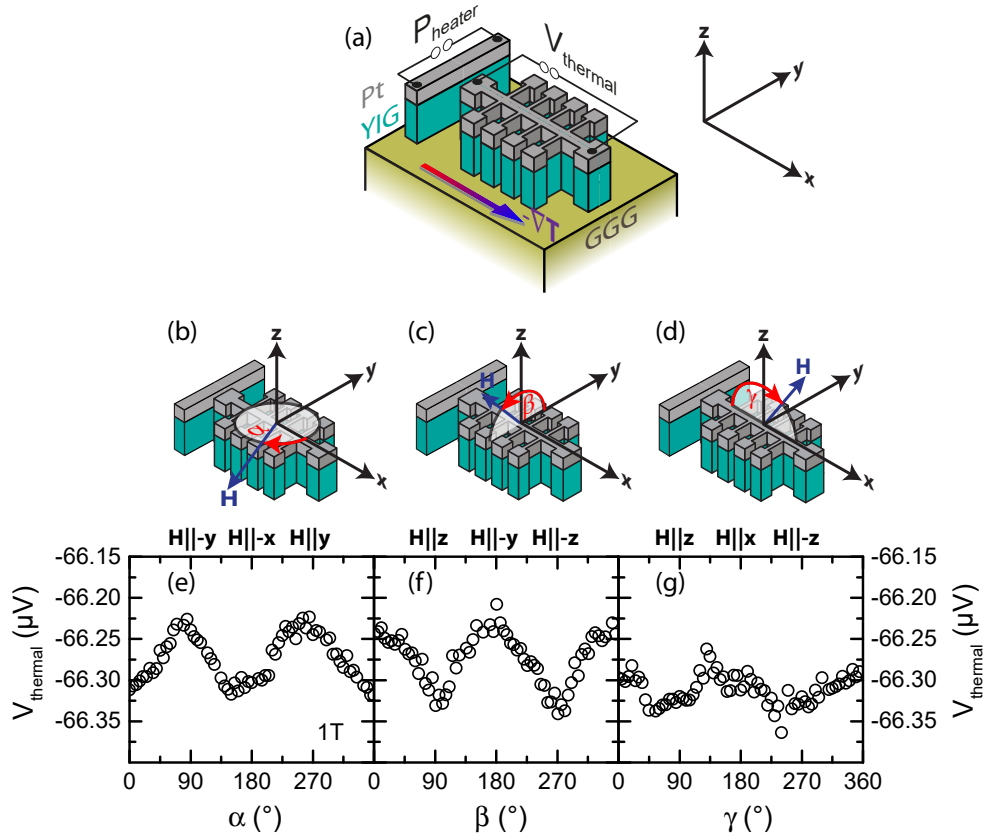


**Figure 3:** (a) Setup of the SNMTP experiments. A YIG|Pt ( $t_F = 40 \text{ nm}/t_N = 4.1 \text{ nm}$ ) thin film is patterned into a Hall bar (width  $w = 250 \mu\text{m}$ , length  $l = 3150 \mu\text{m}$ ). An additional heater strip is defined along  $y$ ,  $d = 250 \mu\text{m}$  beyond the top of the Hall bar. By applying an electric current with power  $P_{\text{heater}}$  to the heater strip, one end of the Hall bar is hotter than the other end that is connected to a heat sink provided by the sample holder (see supplementary information for details), leading to a temperature gradient  $-\nabla T$  along  $x$ . (b)-(d) The magnetization vector  $\mathbf{M}$  of the YIG layer is rotated by an external magnetic field  $\mu_0 H = 1 \text{ T}$  in three different rotation planes spanned by  $(x, y)$  (panel (b)),  $(y, z)$  (panel (c)) and  $(x, z)$  (panel (d)). The measured thermal voltage  $V_{\text{thermal}}$  for all three geometries and  $P_{\text{heater}} = 286 \text{ mW}$  (or  $\Delta T = 18.0 \text{ K}$  along the Hall bar) is depicted in panels (e) for the  $(x, y)$ -plane, (f) for the  $(y, z)$ -plane and (g) for the  $(x, z)$ -plane.

circuit conditions, with a relative signal amplitude of  $|\Delta V_{\text{thermal}}/V_{\text{thermal}}| = (1.5 \pm 0.3) \times 10^{-3}$ , see Fig. 3(e). We reproduced this behavior for full  $360^\circ$  rotations of the applied field in the sample plane spanned by  $\mathbf{x}$  and  $\mathbf{y}$ , leading to a  $\sin^2(\alpha)$  behavior of  $V_{\text{thermal}}$  with minima for short-circuit boundary conditions ( $\alpha = 0^\circ, 180^\circ$ ), and maxima for open boundary conditions ( $\alpha = 90^\circ, 270^\circ$ ). We can also switch the boundary conditions by rotating the magnetic field in the (normal) plane spanned by  $\mathbf{y}$  and  $\mathbf{z}$ , see Fig. 3(f). Starting at  $\beta = 0^\circ$  from  $\mathbf{H} \parallel \mathbf{y}$  (open boundary conditions), the thermal voltage decreases while rotating  $\mathbf{H}$  towards  $\mathbf{z}$  ( $\beta = 90^\circ$ , short-circuit boundary conditions) and the minimal and maximal levels of  $V_{\text{thermal}}$  coincide with the ones obtained in the first geometry. Rotating  $\mathbf{H}$  out-of-plane perpendicular to  $\mathbf{y}$  [Fig. 3(g)], the signal is almost constant and coincides with the lower signal levels observed for the other rotation planes. This is exactly the behavior expected from Eq. (1), since  $\mathbf{H} \perp \mathbf{s}$  is fulfilled for every magnetization orientation in this rotation geometry, causing a maximum spin Nernst spin current flow. Using  $\lambda = 1.5 \text{ nm}$ ,  $\theta_{\text{SH}} = 0.11$  and  $\text{Re}(G) = 4 \times 10^{14} \Omega^{-1}\text{m}^{-2}$  [26] in Eq. (2), the observed  $\Delta V_{\text{thermal}}/V_{\text{thermal}} = -1.5 \times 10^{-3}$  corresponds to a spin Nernst angle of  $\theta_{\text{SN}} = -0.20$  for Pt. Our first principles calculations for the spin transport in Pt confirm the relative sign and suggest  $\theta_{\text{SH}}/\theta_{\text{SN}} = -0.9$  (see SI). This is in fair agreement with  $\theta_{\text{SH}}/\theta_{\text{SN}}(\text{exp.}) = -0.5$ . We repeated our measurements for different heating powers between 100 mW and 286 mW as well as for two different magnetic field values. The relative amplitude of the modulation of the thermal voltage does not depend on both heating power and external magnetic field, as expected (see SI). Note that the observed field dependence excludes interference by the spin Seebeck effect [6, 7, 8].

In summary, we report an SNMTP signal in Pt|YIG hybrids proportional to an in-plane temperature gradient that reveals the spin Nernst effect in Pt, thereby opening a new strategy for the thermal generation of spin currents. The spin Nernst and spin Hall angles are of equal magnitude in Pt but of opposite sign, as corroborated by first principle calculations. With the observation of the spin Nernst effect, the “zoo” of magneto-thermo-galvanic effects is complete. We anticipate that this spin Nernst magneto-thermopower will play an eminent role in the emerging field of spin caloritronics, in particular concerning the development of spintronic devices utilizing ubiquitous temperature gradients e.g. from Joule heating hot spots.

## 2 Methods summary

In our experiments, an Yttrium Iron Garnet ( $\text{Y}_3\text{Fe}_5\text{O}_{12}$ , YIG) thin film was epitaxially grown on a (111)-oriented Gadolinium Gallium Garnet ( $\text{Gd}_3\text{Ga}_5\text{O}_{12}$ , GGG) substrate by pulsed laser deposition, covered in-situ with Pt by electron beam evaporation [25]. The YIG film is an insulating ferrimagnet with a saturation magnetization of 120 kA/m. The Pt layer is polycrystalline with a resistivity of 430 n $\Omega$ m at room temperature. The thicknesses of the YIG and Pt layers were determined by x-ray reflectometry as  $t_{\text{F}} = (40 \pm 2)$  nm and  $t_{\text{N}} = (4.1 \pm 0.2)$  nm, respectively. The  $5 \times 5$  mm<sup>2</sup> sample is patterned into a Hall bar with an additional heating strip as shown in Fig. 3(a). For temperature differences  $\Delta T \leq 18.0$  K between both ends of the Hall bar, the voltage signal  $V_{\text{thermal}}$  is measured while rotating a magnetic field of constant magnitude  $\mu_0 H = 1$  T in different planes.  $\mu_0 H$  is much larger than the saturation field of YIG to ensure the alignment of the magnetization vector  $\mathbf{M}$  of the FMI parallel to the external field even in the presence of magnetic and shape anisotropies. More details on the experimental methods are given in the SI.

## 3 Acknowledgments

S.M., M.A., S.G., H.H., R.G. and S.T.B.G. thank Andreas Erb for the preparation of the stoichiometric YIG target and Thomas Brenninger for technical support. Y.-T.C. and G.E.W.B. acknowledge funding by FOM (Stichting voor Fundamenteel Onderzoek der Materie), EU- ICT-7 “INSPIN”, and Grant-in-Aid for Scientific Research (Grant Nos. 25247056, 25220910, 26103006). All authors acknowledge funding via the DFG Priority program 1538 “Spin-Caloric Transport” (Projects GO 944/4, BA 2954/2 and EB 154/25).

## 4 Author Contributions

S.M. designed the sample layout and carried out the experiments. S.M., Y.-T.C., G.E.W.B., R.G. and S.T.B.G. developed the explanation of the SNMTP effect. S.G. supervised the sample growth. Y.-T.C. and G.E.W.B. developed the theoretical framework and S.W., D.K. and H.E. performed first-principles calculations of the relevant spin-caloric transport coefficients. S.T.B.G. supervised the experiments. The manuscript was written by S.M., M.A. and S.T.B.G. All authors discussed and participated in writing the manuscript under the guidance of S.M. and G.E.W.B.

## 5 Affiliations

**Walther-Meißner-Institut, Bayerische Akademie der Wissenschaften,  
Walther-Meißner-Straße 8, 85748 Garching, Germany**

Sibylle Meyer, Matthias Althammer, Stephan Geprägs, Hans Huebl, Rudolf Gross and Sebastian T. B. Goennenwein

**Physik-Department, Technische Universität München, 85748 Garching, Germany**

Sibylle Meyer, Hans Huebl, Rudolf Gross and Sebastian T.B. Goennenwein

**Kavli Institute of NanoScience, Delft University of Technology, Lorentzweg 1, 2628 CJ Delft, The Netherlands**

Yan-Ting Chen and Gerrit E. W. Bauer

**RIKEN Center for Emergent Matter Science (CEMS), 2-1 Hirosawa, Wako, Saitama 351-0198, Japan**

Yan-Ting Chen

**Department Chemie, Physikalische Chemie, Universität München, Butenandtstraße 5-13, 81377 München, Germany**

Sebastian Wimmer, Diemo Ködderitzsch and Hubert Ebert

**Nanosystems Initiative Munich (NIM), Schellingstraße 4, 80799 München, Germany**

Hans Huebl, Rudolf Gross and Sebastian T. B. Goennenwein

**Institute for Materials Research, Tohoku University, Sendai, Miyagi 980-8577, Japan**

Gerrit E. W. Bauer

**WPI Advanced Institute for Materials Research, Tohoku University, Sendai 980-8577, Japan**

Gerrit E. W. Bauer

## 6 Competing Interests Statement

The authors declare that they have no competing financial interests. Supplementary information accompanies this paper online.

## 7 Corresponding author

Correspondence and requests for materials should be addressed to S.T.B.G.

## 8 Supplementary Information (SI)

### 8.1 Theory of the spin Nernst magnetothermopower

Here we present a theoretical analysis of the SNMTP effect in N|FMI bilayer systems in terms of a non-equilibrium proximity effect caused by the simultaneous action of the spin Nernst effect (SNE) and the inverse spin Hall effect (ISHE). This effect scales like the product of the spin Hall and spin Nernst angle, and is modulated by the magnetization direction in YIG via the spin transfer at the N|FMI interface. Our explanation is a generalization of that of the spin Hall magnetoresistance [23, 27], and is based on the spin-diffusion approximation in the N layer in the presence of spin-orbit interaction [28] and quantum mechanical boundary conditions at the interface in terms of the spin-mixing conductance [22, 29].

We consider a N|FMI bilayer homogeneous in the x-y plane ( $z = 0$  defines the interface), and calculate the spin accumulation, spin currents and finally the measured charge currents that are compared with the experimental SNMTP. We also find that the imaginary part of the spin-mixing conductance generates an anomalous Nernst effect (ANE) (that appears to be too small to be observable, however).

The spin current density in the non-relativistic limit

$$\mathbf{j}_s = -en \frac{\langle \mathbf{v} \times \boldsymbol{\sigma} + \boldsymbol{\sigma} \times \mathbf{v} \rangle}{2} = (\mathbf{j}_{s,x}, \mathbf{j}_{s,y}, \mathbf{j}_{s,z})^T = (\mathbf{j}_s^x, \mathbf{j}_s^y, \mathbf{j}_s^z) \quad (3)$$

is a second-order tensor (in units of the charge current density  $\mathbf{j}_c = -en \langle \mathbf{v} \rangle$ ), where  $-e$  ( $e > 0$ ) is the electron charge,  $n$  is the density of the electrons,  $\mathbf{v}$  is the velocity operator,  $\boldsymbol{\sigma}$  is the vector of Pauli spin matrices, and  $\langle \dots \rangle$  denotes the thermodynamic expectation value for a non-equilibrium state. The row vectors  $\mathbf{j}_{s,i} = -en \langle \mathbf{v} \times \sigma_i + \sigma_i \times \mathbf{v} \rangle / 2$  are the spin current densities polarized in the  $\mathbf{i}$  direction, while the column vectors  $\mathbf{j}_s^j = -en \langle v_j \times \boldsymbol{\sigma} + \boldsymbol{\sigma} \times v_j \rangle / 2$  denote the spin current densities with polarization  $\eta$  flowing in the  $\mathbf{j}$  direction. On the other hand, the heat current reads  $\mathbf{j}_h = n \langle (E - E_F) \mathbf{v} \rangle$ , where  $E$  stands for the energy of the particle,  $E_F$  represents the Fermi energy. Ohm's Law for metals with spin-orbit interactions can be summarized by the relation between thermodynamic driving forces and currents that reflects the Onsager

reciprocity by the symmetry of the response matrix [27, 28]

$$\begin{pmatrix} \mathbf{j}_c \\ \mathbf{j}_h \\ \mathbf{j}_{s,x} \\ \mathbf{j}_{s,y} \\ \mathbf{j}_{s,z} \end{pmatrix} = \sigma \begin{pmatrix} 1 & ST & \theta_{\text{SH}\mathbf{x}\times} & \theta_{\text{SH}\mathbf{y}\times} & \theta_{\text{SH}\mathbf{z}\times} \\ ST & L_0 T^2 & ST\theta_{\text{SN}\mathbf{x}\times} & ST\theta_{\text{SN}\mathbf{y}\times} & ST\theta_{\text{SN}\mathbf{z}\times} \\ \theta_{\text{SH}\mathbf{x}\times} & ST\theta_{\text{SN}\mathbf{x}\times} & 1 & 0 & 0 \\ \theta_{\text{SH}\mathbf{y}\times} & ST\theta_{\text{SN}\mathbf{y}\times} & 0 & 1 & 0 \\ \theta_{\text{SH}\mathbf{z}\times} & ST\theta_{\text{SN}\mathbf{z}\times} & 0 & 0 & 1 \end{pmatrix} \begin{pmatrix} \nabla\mu_0/e \\ -\nabla T/T \\ \nabla\mu_{s,x}/(2e) \\ \nabla\mu_{s,y}/(2e) \\ \nabla\mu_{s,z}/(2e) \end{pmatrix} \quad (4)$$

where  $\boldsymbol{\mu}_s = (\mu_{sx}, \mu_{sy}, \mu_{sz})^T - \mu_0 \mathbf{1}$  is the spin accumulation, i.e. the spin-dependent chemical potential relative to the electrochemical potential  $\mu_0$ ,  $\sigma$  is the electrical conductivity,  $S = -eL_0 T \partial_E(\ln(\sigma))|_{E_F}$  is the Seebeck coefficient,  $L_0 = (\pi^2/3)(k_B/e)^2$  is the Lorenz constant with  $k_B$  the Boltzmann constant,  $\theta_{\text{SH}}$  ( $\theta_{\text{SN}}$ ) is the spin Hall (Nernst) angle, and  $\times$  denotes the vector cross product operating on the driving forces. The spin Hall (Nernst) effect is represented by the lower non-diagonal elements that generate the spin currents in the presence of an applied electric field (temperature gradient), while the inverse spin Hall (Nernst) effect is governed by elements above the diagonal that connect the gradients of the spin accumulations to the charge (heat) current density. In this study, we focus on the charge current generated by an external temperature gradient and thus the driving force is chosen to be a temperature gradient in the  $\mathbf{x}$  direction  $\nabla T = \mathbf{x} \partial_x T$  which drives a charge current  $j_{c0} \mathbf{x} = -\sigma S \partial_x T \mathbf{x}$  via the Seebeck effect.

The spin accumulation  $\mu_s$  is obtained from the spin-diffusion equation in the normal metal

$$\nabla^2 \boldsymbol{\mu}_s = \frac{\boldsymbol{\mu}_s}{\lambda^2} \quad (5)$$

where the spin-diffusion length  $\lambda = \sqrt{D\tau_{\text{sf}}}$  is expressed in terms of the charge diffusion constant  $D$  and spin-flip relaxation time  $\tau_{\text{sf}}$  [30]. For films with thickness  $t_N$  in the  $\mathbf{z}$  direction,

$$\boldsymbol{\mu}_s(z) = \mathbf{A} e^{-z/\lambda} + \mathbf{B} e^{z/\lambda} \quad (6)$$

where the constant column vectors  $\mathbf{A}$  and  $\mathbf{B}$  are determined by the boundary conditions at the interfaces. According to Eq. (4), the spin current in N consists of diffusion and spin Nernst drift contributions. Since we are considering a system homogeneous in the x-y plane, we focus on the spin current density flowing in the  $\mathbf{z}$  direction,

$$\mathbf{j}_s^z(z) = \frac{\sigma}{2e} \partial_z \boldsymbol{\mu}_s - j_{s0}^{\text{SN}} \mathbf{y}, \quad (7)$$

where  $j_{s0}^{\text{SN}} = -\theta_{\text{SN}}\sigma S\partial_x T$  is the bare spin Nernst current, i.e., the spin current generated directly by the SNE. The boundary conditions require that  $\mathbf{j}_s^z$  is continuous at the interfaces  $z = t_N$  and  $z = 0$ . The spin current at a vacuum (V) interface vanishes,  $\mathbf{j}_s(V) = 0$ . The spin current density  $\mathbf{j}_s^{(\text{F})}$  at a magnetic interface is governed by the spin accumulation and spin-mixing conductance:[22]

$$e\mathbf{j}_s^{(\text{F})}(\mathbf{m}) = G_r\mathbf{m} \times (\mathbf{m} \times \boldsymbol{\mu}_s) + G_i(\mathbf{m} \times \boldsymbol{\mu}_s) \quad (8)$$

where  $\mathbf{m} = (m_x, m_y, m_z)^T$  is a unit vector along the magnetization and  $G = G_r + \imath G_i$  the complex spin-mixing interface conductance per unit area and  $\imath = \sqrt{-1}$ . The imaginary part  $G_i$  can be interpreted as an effective exchange field acting on the spin accumulation. A positive current in Eq. (8) corresponds to up spins flowing from the FMI towards N. With these boundary conditions we determine the coefficients  $\mathbf{A}$  and  $\mathbf{B}$ , which leads to the spin accumulation in the bilayer system

$$\boldsymbol{\mu}_s(z) = \mathbf{y}\mu_s^0 \frac{\sinh \frac{2z-t_N}{2\lambda}}{\sinh \frac{t_N}{2\lambda}} - \mathbf{j}_s^{(\text{F})}(\mathbf{m}) \frac{2e\lambda \cosh \frac{z-t_N}{\lambda}}{\sigma \sinh \frac{t_N}{\lambda}} \quad (9)$$

where  $\mu_s^0 = (2e\lambda/\sigma)\mathbf{j}_{s0}^{\text{SN}} \tanh(t_N/2\lambda)$  is the spin accumulation at the interface in the absence of spin transfer, i.e., when  $G = 0$ . Following Ref. [27], the spin accumulation reads

$$\begin{aligned} \frac{\boldsymbol{\mu}_s(z)}{\mu_s^0} &= \mathbf{y} \frac{\sinh \frac{2z-t_N}{2\lambda}}{\sinh \frac{t_N}{2\lambda}} \\ &- [\mathbf{m} \times (\mathbf{m} \times \mathbf{y})\text{Re} + (\mathbf{m} \times \mathbf{y})\text{Im}] \frac{2\lambda G}{\sigma + 2\lambda G \coth \frac{t_N}{\lambda}} \frac{\cosh \frac{z-t_N}{\lambda}}{\sinh \frac{t_N}{\lambda}} \end{aligned} \quad (10)$$

which leads to the distributed spin current in the N

$$\begin{aligned} \frac{\mathbf{j}_s^z(z)}{j_{s0}^{\text{SN}}} &= \mathbf{y} \frac{\cosh \frac{2z-t_N}{2\lambda} - \cosh \frac{t_N}{2\lambda}}{\cosh \frac{t_N}{2\lambda}} \\ &- [\mathbf{m} \times (\mathbf{m} \times \mathbf{y})\text{Re} + (\mathbf{m} \times \mathbf{y})\text{Im}] \frac{2\lambda G \tanh \frac{t_N}{2\lambda}}{\sigma + 2\lambda G \coth \frac{t_N}{\lambda}} \frac{\sinh \frac{z-t_N}{\lambda}}{\sinh \frac{t_N}{\lambda}} \end{aligned} \quad (11)$$

The ISHE drives a charge current in the x-y plane by the diffusion spin current component flowing along the  $\mathbf{z}$  direction. The total longitudinal (along  $\mathbf{x}$ ) and

transverse or Hall (along  $\mathbf{y}$ ) charge currents become

$$\frac{\mathbf{j}_{c,\text{long}}(z)}{j_{c0}} = 1 + \theta_{\text{SH}}\theta_{\text{SN}} \left[ \frac{\cosh \frac{2z-t_{\text{N}}}{2\lambda}}{\cosh \frac{t_{\text{N}}}{2\lambda}} + (1 - m_y^2) \text{Re} \frac{2\lambda G \tanh \frac{t_{\text{N}}}{2\lambda}}{\sigma + 2\lambda G \coth \frac{t_{\text{N}}}{\lambda}} \frac{\sinh \frac{z-t_{\text{N}}}{\lambda}}{\sinh \frac{t_{\text{N}}}{\lambda}} \right] \quad (12)$$

$$\frac{\mathbf{j}_{c,\text{trans}}(z)}{j_{c0}} = \theta_{\text{SH}}\theta_{\text{SN}}(m_x m_y \text{Re} - m_z \text{Im}) \frac{2\lambda G \tanh \frac{t_{\text{N}}}{2\lambda}}{\sigma + 2\lambda G \coth \frac{t_{\text{N}}}{\lambda}} \frac{\sinh \frac{z-t_{\text{N}}}{\lambda}}{\sinh \frac{t_{\text{N}}}{\lambda}} \quad (13)$$

For an open-circuit configuration for the charge current, the observable in the experiment (thermal voltage) is expressed as an electric field  $\mathbf{E}_{\text{th}} = E_{\text{th},x}\mathbf{x} + E_{\text{th},y}\mathbf{y}$  which compensates  $j_{c,\text{long}}$  and  $j_{c,\text{trans}}$ :

$$E_{\text{th},x} = \left[ 1 + \theta_{\text{SH}}\theta_{\text{SN}} \left[ \frac{\cosh \frac{2z-t_{\text{N}}}{2\lambda}}{\cosh \frac{t_{\text{N}}}{2\lambda}} + (1 - m_y^2) \text{Re} \frac{2\lambda G \tanh \frac{t_{\text{N}}}{2\lambda}}{\sigma + 2\lambda G \coth \frac{t_{\text{N}}}{\lambda}} \frac{\sinh \frac{z-t_{\text{N}}}{\lambda}}{\sinh \frac{t_{\text{N}}}{\lambda}} \right] \right] S \partial_x T$$

$$E_{\text{th},y} = \theta_{\text{SH}}\theta_{\text{SN}}(m_x m_y \text{Re} - m_z \text{Im}) \frac{2\lambda G \tanh \frac{t_{\text{N}}}{2\lambda}}{\sigma + 2\lambda G \coth \frac{t_{\text{N}}}{\lambda}} \frac{\sinh \frac{z-t_{\text{N}}}{\lambda}}{\sinh \frac{t_{\text{N}}}{\lambda}} S \partial_x T. \quad (14)$$

Averaging the electric field component along  $\mathbf{x}$  over the film thickness  $z$ , we obtain

$$\overline{E_{\text{th},x}} = [S + \Delta S_0 + \Delta S_1(1 - m_y^2)] \partial_x T \quad (15)$$

which includes

$$\Delta S_0 = S \theta_{\text{SH}}\theta_{\text{SN}} \frac{2\lambda}{t_{\text{N}}} \tanh \frac{t_{\text{N}}}{2\lambda} \quad (16)$$

$$\Delta S_1 = -S \theta_{\text{SH}}\theta_{\text{SN}} \frac{\lambda}{t_{\text{N}}} \text{Re} \frac{2\lambda G \tanh^2 \frac{t_{\text{N}}}{2\lambda}}{\sigma + 2\lambda G \coth \frac{t_{\text{N}}}{\lambda}} \quad (17)$$

The voltages detected in our experiments are linked to the electric field components in Eq. (15) via

$$V_{\text{thermal}} = - \int \overline{E_{\text{th},x}}(\mathbf{x}) d\mathbf{x} \quad (18)$$

Thus, the spin current generated by the SNE generates additional contributions  $\Delta S_0$  and  $\Delta S_1$  to the Seebeck coefficient. For longitudinal thermopower measurements, we therefore expect a magnetization orientation dependent contribution to  $S$  and thus to the thermopower voltage  $V_{\text{thermal}}$  proportional to  $\Delta S_1(1 - m_y^2)$ . This is caused by the spin transport across the N|FMI interface described mainly by  $G_r$ . Comparing Eq. (15) with the longitudinal SMR (cf. Ref. [27]), we find the same magnetization orientation dependence proportional to  $m_y^2$ . We thus

expect that the SNMTP has a similar fingerprint as the SMR, with modulations in  $V_{\text{thermal}}$  when the magnetization of the FMI (the YIG) is rotated in planes spanned by  $\mathbf{x}$  and  $\mathbf{y}$  as well as in planes spanned by  $\mathbf{z}$  and  $\mathbf{y}$ , while we expect no modulations in  $V_{\text{thermal}}$  when the magnetization of the FMI is rotated in  $(\mathbf{x}, \mathbf{z})$  plane.

## 8.2 First principles description of the spin Nernst effect

In an independent theoretical effort, we derive the magnitude of the spin Hall and the spin Nernst angles in platinum from first principles. Considering both an electric field  $\mathbf{E}$  and a temperature gradient  $\nabla T$  as generating forces for a spin-polarized current

$$\mathbf{J}^s = -e\mathcal{L}^{\text{sc}}\mathbf{E} - \mathcal{L}^{\text{sq}}\nabla T/T \quad (19)$$

the tensors  $\mathcal{L}^{\text{sc}}$  and  $\mathcal{L}^{\text{sq}}$  describe the response of the system under investigation. For a spin-polarization axis along  $\xi$ , the spin current along  $\mu$ , and the electric field along  $\nu$ , with  $\mu(\nu, \xi) \in \{x, y, z\}$ , one obtains for the former

$$\mathcal{L}_{\mu\nu}^{\text{sc},\xi}(T) = -\frac{1}{e} \int dE \sigma_{\mu\nu}^{\text{sc},\xi}(E) D(E, T), \quad (20)$$

with  $D(E, T) = \left(-\frac{\partial f(E, T)}{\partial E}\right)$ ,  $f(E, T)$  the Fermi function and the energy-dependent spin conductivity  $\sigma_{\mu\nu}^{\text{sc},\xi}(E)$  which is obtained by applying the Kubo-Středa linear response formalism and an appropriate form of the spin current density operator [31, 32] in combination with the relativistic KKR (Korringa-Kohn-Rostocker) band structure method [33, 34, 35, 32].

In analogy to the relation between the transport coefficient  $L_{\mu\nu}^{\text{cq}}(T)$  and the energy-dependent electrical conductivity  $\sigma_{\mu\nu}^{\text{cc}}(E)$  [36], the temperature-dependent spin transport coefficient  $\mathcal{L}_{\mu\nu}^{\text{sq},\xi}(T)$  is expressed in terms of the energy-dependent spin conductivity  $\sigma_{\mu\nu}^{\text{sc},\xi}(E)$ :

$$\mathcal{L}_{\mu\nu}^{\text{sq},\xi}(T) = -\frac{1}{e} \int dE \sigma_{\mu\nu}^{\text{sc},\xi}(E) D(E, T) (E - E_F), \quad (21)$$

with  $E_F$  the Fermi energy.

Considering a temperature gradient  $\nabla T$  without an external electric field  $\mathbf{E}$ , the electric current density

$$\mathbf{j}^c = -eL^{\text{cc}}\mathbf{E} - L^{\text{cq}}\nabla T/T \quad (22)$$

vanishes when open-circuit conditions are imposed. Equation (22) implies that an internal electric field

$$\mathbf{E} = -\frac{1}{eT}(L^{\text{cc}})^{-1}L^{\text{cq}}\nabla T = S\nabla T \quad (23)$$

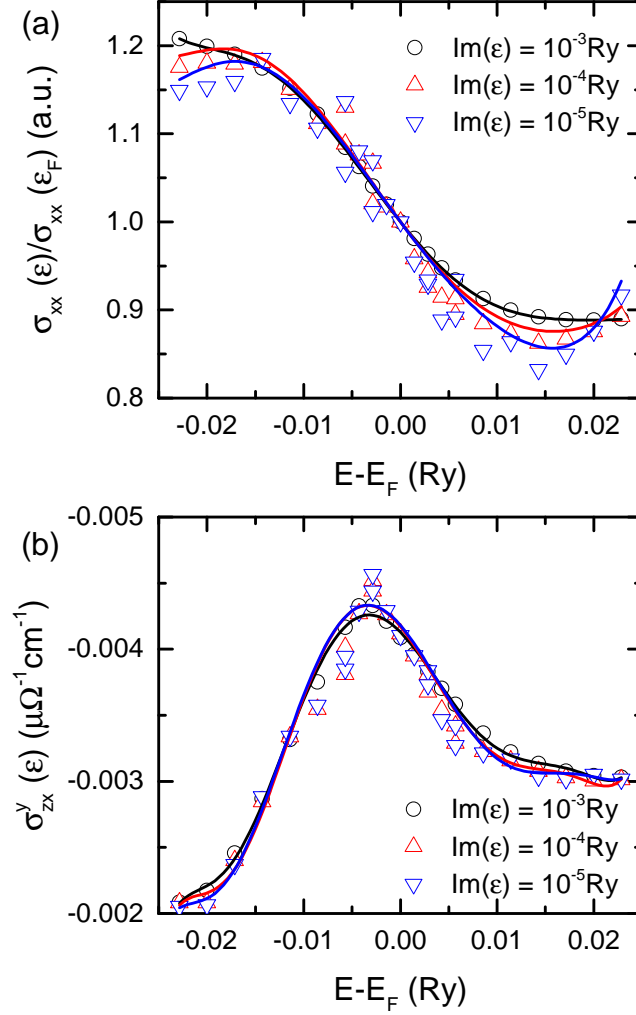
compensates the charge imbalance induced by  $\nabla T$ , where  $S$  is the thermo (magneto) electric tensor. The ratios  $\mathcal{L}_{\text{zx}}^{\text{sc},y}/L_{\text{xx}}^{\text{cc}} = \theta_{\text{SH}}$ , i.e. the spin Hall angle ( $\theta_{\text{SH}}$ ), and  $\mathcal{L}_{\text{zx}}^{\text{sq},y}/L_{\text{xx}}^{\text{cq}} = \theta_{\text{SN}}$ , i.e. the corresponding spin Nernst angle ( $\theta_{\text{SN}}$ ), express the efficiency of conversion of a longitudinal charge current density into a transverse spin current density, generated by an electric field or a temperature gradient, respectively (see Eq. (4)). Using Eq. (23) and the expressions for the electrical and thermoelectrical conductivities in terms of Eqs. (20) and (21),  $\sigma_{\text{xx}}$  ( $\sigma_{\text{zx}}^y$ ) =  $-eL_{\text{xx}}^{\text{cc}}$  ( $-e\mathcal{L}_{\text{zx}}^{\text{sc},y}$ ) and  $\alpha_{\text{xx}}$  ( $\alpha_{\text{zx}}^y$ ) =  $-\frac{1}{T}L_{\text{xx}}^{\text{cq}}$  ( $-\frac{1}{T}\mathcal{L}_{\text{zx}}^{\text{sq},y}$ ), their (temperature-dependent) ratio can be written as

$$\frac{\theta_{\text{SH}}}{\theta_{\text{SN}}}(T) = \frac{\sigma_{\text{zx}}^y(T) \alpha_{\text{xx}}(T)}{\sigma_{\text{xx}}(T) \alpha_{\text{zx}}^y(T)} = -S_{\text{xx}}(T) \frac{\sigma_{\text{zx}}^y(T)}{\alpha_{\text{zx}}^y(T)}. \quad (24)$$

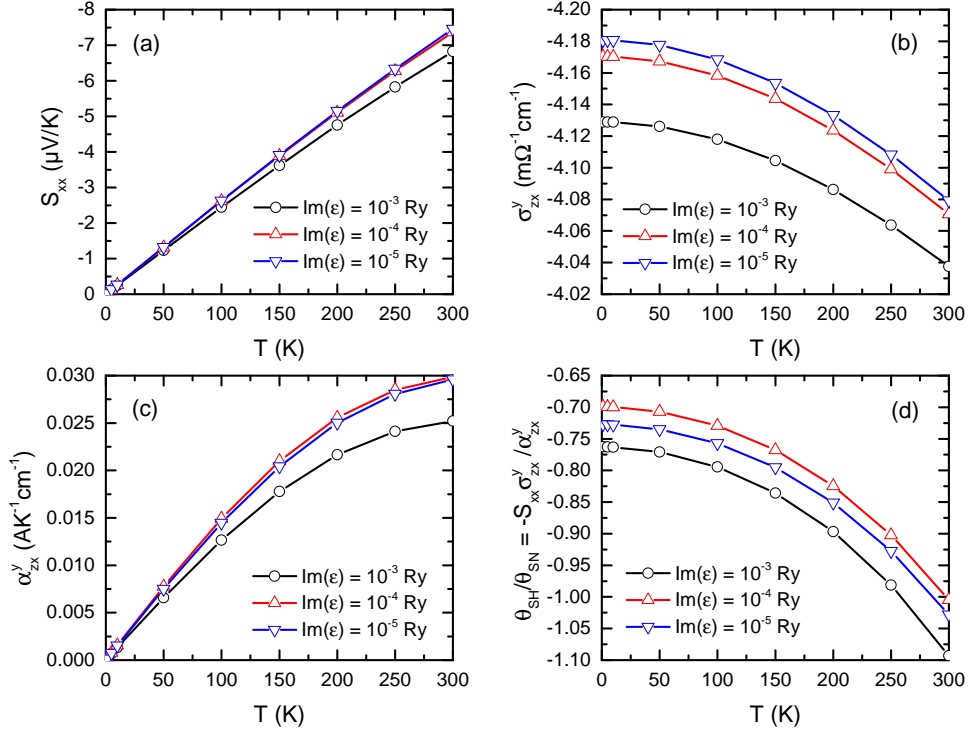
Following the notation of the previous section,  $\sigma_{xx}$  corresponds to  $\sigma$  in Eq. (4),  $\sigma_{zx}^y$  to  $\theta_{\text{SH}}\sigma$ ,  $\alpha_{xx}$  to  $-\sigma S$  and  $\alpha_{zx}^y$  to  $-\theta_{\text{SN}}\sigma S$ . The energy-dependent conductivities entering Eqs. (20) and (21) and the corresponding expressions for the longitudinal transport coefficients were calculated for energies  $\varepsilon = E + i\eta$  with a small imaginary part  $\eta$ . This is necessary due to the fact that for a pure metal, the longitudinal electrical conductivity ( $\sigma_{xx}$ ) and accordingly also the Peltier coefficient ( $\alpha_{xx}$ ) diverge. However, the ratio of the latter two, the Seebeck coefficient  $S_{\text{xx}} = -\sigma_{\text{xx}}^{-1}\alpha_{\text{xx}}$  does not depend significantly on  $\eta$ , as can be seen from Fig. 5 (top left). For the transverse quantities, i.e the spin Hall and spin Nernst conductivities, with increasing number of  $k$ -points (here a regular sampling of the Brillouin zone was used, with about 130 million mesh points) and  $\text{Im}(\varepsilon) \rightarrow 0$  the calculations converge to a finite result, the so-called intrinsic contributions to  $\sigma_{\text{zx}}^y$  and  $\alpha_{\text{zx}}^y$ .

Figure 4 shows the calculated values of  $\sigma_{\text{xx}}(\varepsilon)$  (top) and  $\sigma_{\text{zx}}^y(\varepsilon)$  (bottom) for  $\text{Im}(\varepsilon) = 10^{-3}$  (black pluses),  $10^{-4}$  (red circles) and  $10^{-5}$  (blue squares), together with polynomial fits. The temperature-dependent Seebeck coefficient, spin Hall conductivity and spin Nernst conductivity subsequently obtained from these are shown in Fig. (5) at the top left, top right and bottom left, respectively.

They were calculated using the fitted  $\sigma(\varepsilon)$  curves from Fig. 4 in the integrands of Eqs. (20) and (21), i.e. without making use of the Sommerfeld approximation. Finally, the ratio of the spin Hall and the spin Nernst angle, expressed by the above quantities as in Eq. (24), is shown as a function of temperature in Fig. (5),



**Figure 4:** Energy dependence of longitudinal charge (a) and transverse spin-polarized conductivity (b),  $\sigma_{xx}(E)$  and  $\sigma_{zx}^y(E)$ , respectively. Calculations were performed at complex energies  $\epsilon = E + i\eta$  for three different values of  $\eta$ . The results for the charge conductivity (a) are normalized by the value at  $\epsilon_F = E_F + i\eta$  with  $E_F$  being the Fermi energy.



**Figure 5:** Temperature dependence of (a) the Seebeck coefficient  $S_{xx}$ , (b) the spin Hall conductivity  $\sigma_{zx}^y$ , (c) the spin Nernst conductivity,  $\alpha_{zx}^y$ , and (d) of the ratio  $\theta_{\text{SH}}/\theta_{\text{SN}}$  as defined in Eq. (24). Results are shown for three different values of  $\eta$ , using the polynomial fits to the calculated values of  $\sigma_{xx}(\epsilon)$  and  $\sigma_{zx}^z(\epsilon)$  (see Fig. 4 and text).

bottom right. As can be seen, for the conventions and definitions chosen here, the two angles have opposite signs for the whole temperature range and for  $T < 250$  K the  $\theta_{\text{SN}}$  is larger than the  $\theta_{\text{SH}}$ .

### 8.3 Experimental methods

The sample used in this study is a YIG|Pt thin film heterostructure. YIG hereby stands for Yttrium Iron Garnet ( $\text{Y}_3\text{Fe}_5\text{O}_{12}$ ). The 40 nm thick YIG layer was epitaxially grown on a 500  $\mu\text{m}$  thick, single crystalline, (111)-oriented Gadolinium Gallium Garnet (GGG,  $\text{Gd}_3\text{Ga}_5\text{O}_{12}$ ) substrate via pulsed laser deposition using a stoichiometric target[25]. The deposition was carried out

in an oxygen atmosphere of  $25 \mu\text{bar}$ , with a laser energy density of  $2 \text{ J/cm}^2$  at the target, and a substrate temperature of  $550 \text{ }^\circ\text{C}$ . The YIG layer is capped in-situ, without breaking the vacuum, with a  $4.1 \text{ nm}$  thick Pt layer via electron beam evaporation at room temperature. The thicknesses of the YIG and Pt layer were determined by high-resolution X-ray reflectometry (HR-XRR) to  $t_F = (40 \pm 2) \text{ nm}$  and  $t_N = (4.1 \pm 0.2) \text{ nm}$ , respectively. High-resolution X-ray diffraction (HR-XRD) measurements confirmed the polycrystallinity of the Pt thin film and revealed no secondary phases.

After pre-characterization, the sample was patterned into a Hall bar structure with the additional on-chip heater strip as sketched in Fig. 6(a) via optical lithography and Ar ion beam milling. The Hall bar has a width of  $w = 250 \mu\text{m}$ , a length of  $l = 3150 \mu\text{m}$  and a contact separation of  $s = 625 \mu\text{m}$ , the heating strip along  $y$  is  $w_h = 250 \mu\text{m}$  wide and  $l_h = 1175 \mu\text{m}$  long, the distance between Hall bar and heating stripe is  $d = 250 \mu\text{m}$ . The sample is mounted onto a massive copper sample holder with one end, using GE 7031 thermally conductive varnish. The other end of the sample (with the heater strip) is connected to a Vespel block, again with GE varnish. In this way, the sample is thermally anchored to the sample holder on one end, and can be heated on the other, thermally 'isolated' end attached to the Vespel. All bonding pads at the Hall bar as well as the heater strip were connected to a printed circuit connector board with  $30 \mu\text{m}$  thick Al wires via wedge bonding. The bonded sample is mounted on a dedicated magnet cryostat dipstick. This dipstick is enclosed in an evacuated steel jacket, such that the sample resides in vacuum. A pressure of  $(5 \pm 1) \times 10^{-6} \text{ mbar}$  within the sample space was kept constant during the experiments.

Our Oxford Instruments 3D vector magnet cryostat, equipped with a variable temperature insert (VTI), allows to apply magnetic fields  $\leq 2 \text{ T}$  in any desired orientation to the sample, while at the same time adjusting the VTI temperature in the range  $2 \text{ K} \leq T \leq 300 \text{ K}$ . In all magneto-transport experiments discussed here, we used external magnetic field magnitudes  $\mu_0 H_{\text{ext}} \geq 500 \text{ mT}$ , which exceed the saturation magnetization  $\mu_0 M_{\text{Sat}}^F \approx 170 \text{ mT}$  of our YIG thin films at room temperature by at least about 3 times [37]. Thus, the magnetization vector  $\mathbf{M}$  of the YIG layer is always aligned parallel to  $\mu_0 \mathbf{H}_{\text{ext}}$ .

### On-chip thermometry

The base temperature of the sample holder (to which the cold end of the sample is anchored) was set to  $220 \text{ K}$  and stabilized using the PID feedback loop of a LakeShore LS340 temperature controller. Using the on-chip thermometry described below, we found that the temperature was stable within fluctuations

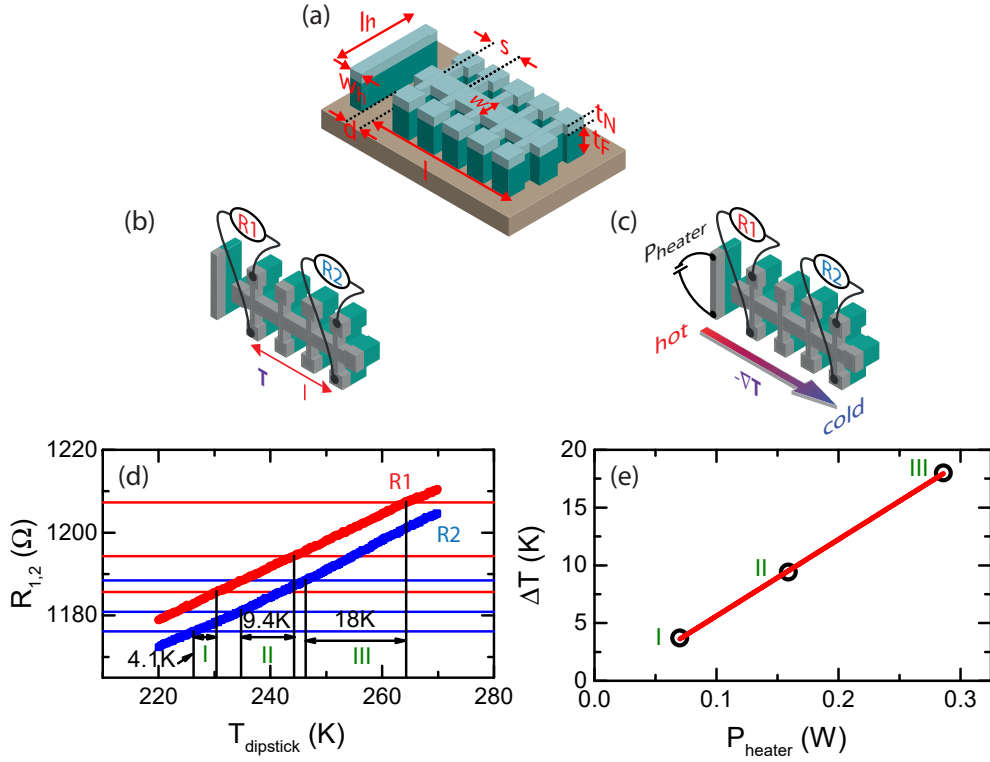


**Figure 6:** (a) *Experimental setup for SNMTP experiments.* A YIG|Pt ( $t_F = 40 \text{ nm}/t_N = 4.1 \text{ nm}$ ) thin film sample is patterned into a Hall bar geometry (width  $w = 250 \mu\text{m}$ , length  $l = 3150 \mu\text{m}$ ). An additional heater strip (width  $w_h = 250 \mu\text{m}$ , length  $l_h = 1175 \mu\text{m}$ ) is defined along  $y$ , separated by  $d = 250 \mu\text{m}$  beyond the top of the Hall bar. (b,c) *Concept of the resistive thermometry:* In a first step (b), the resistance vs. temperature curves  $R_1(T)$  and  $R_2(T)$  along two transverse contact pairs are measured, while no power is applied to the heater. Here, the sample temperature is homogeneous and given by the dipstick temperature  $T_{\text{dipstick}}$ .  $R_1(T)$  and  $R_2(T)$  serve as calibration curves for the thermometry. Afterwards (c), the dipstick temperature is kept constant ( $T_{\text{base}} = 220 \text{ K}$ ) while the electric power  $P_{\text{heater}}$  at the OCH is increased stepwise.  $R_1$  and  $R_2$  are now taken as a function of  $P_{\text{heater}}$ . Panel (d) shows both the calibration curves  $R_1(T)$  and  $R_2(T)$  and the heater dependent resistance values (horizontal lines). From those calibration curves, the local temperatures can be calculated as a function of  $P_{\text{heater}}$ . Here, we show three different heater powers (I)  $P_{\text{heater}} = 70 \text{ mW}$ , (II)  $P_{\text{heater}} = 159 \text{ mW}$  and (III)  $P_{\text{heater}} = 286 \text{ mW}$ . The extracted temperature differences  $\Delta T$  along the Hall bar as a function of  $P_{\text{heater}}$  are shown in (e).

of  $\Delta T_{\text{base}} = 3 \text{ mK}$  (given by the temperature fluctuations displayed by the temperature controller) after a thermalization time of six hours. By applying heating currents of up to 20 mA to the heater strip next to the Hall bar by means of an Agilent B2900A Precision Source Measure Unit, corresponding to heating powers up to 286 mW, we created a temperature gradient along the Hall bar direction  $\mathbf{x}$ . The temperature profile along the Hall bar was determined by resistive thermometry (see Fig. 6) along two transverse Hall bar contact pairs separated by a distance of  $l_1 = 2500 \mu\text{m}$  using two Keithley K2400 Source Measure Units and currents of  $10 \mu\text{A}$  [cf. Fig. 6(a)]. In order to calibrate our 'on-chip Pt temperature sensors', we first stabilized the sample (viz the sample holder) temperature to 220 K (no heating current applied to the on-chip heater strip) and measured  $R_{1,2}(T)$  at either end of the Hall bar while sweeping the sample temperature with 1 K/min up to 270 K using the temperature control of the dipstick just described. These resistance vs. temperature curves, shown in Fig. 6 (c) are used as calibration curves. After that, we again cooled the sample down to the base temperature of 220 K and determined  $R_{1,2}(P_{\text{heater}})$  while applying different heating powers up to 286 mW [cf. Fig. 6 (b)]. Comparing  $R_{1,2}(P_{\text{heat}})$  with the calibration curves taken before allow to recalculate the local sample temperature, such that a temperature profile of the sample with an experimental error of  $\Delta T_{\text{local}} \approx 0.4 \text{ K}$  [see Fig. 6 (d)] is established. Please note that the error of  $\Delta T_{\text{local}} \approx 0.4 \text{ K}$  is determined at the platinum strips by resistive thermometry, while the fluctuation  $\Delta T_{\text{base}} = 3 \text{ mK}$  of the heat bath was determined by a Cernox temperature sensor at the sample holder.

### Power scaling

We find a linear dependence of the temperature difference along the Hall bar on the applied heating power. Accordingly, we expect an almost linear scaling between thermopower and applied heater power [38]. The maximum generated temperature difference between the contacts separated by the distance  $l_1$  was found to be 18.0 K for  $P_{\text{heater}} = 286 \text{ mW}$ . In Fig. 7, we show the thermopower voltage taken along the Hall bar direction for different, constant heating currents applied to the OCH. Although the presence of a magnetic field usually is not required for the determination of the thermoelectric voltages, we applied a magnetic field of 1 T along  $\mathbf{x}$  in these experiments, in order to orient the magnetization of the YIG film and thus induce a reproducible contribution from the SNMTP. As evident from Fig. 7, we find an increase in the absolute value of  $V_{\text{thermal}}$  with increasing  $I_{\text{heater}}$ , as expected for a thermopower effect from  $V_{\text{therm}} = S\Delta T$ . For the highest heater current applied,

we extract  $S = -3.7\mu\text{V}/\text{K}$  using  $\Delta T = 18.0\text{K}$ . With respect to the average sample temperature  $\bar{T} = (T_{\text{hot}} - T_{\text{cold}})/2 = 255.4\text{K}$  extracted from the resistive thermometry shown above,  $S$  is in excellent agreement with the literature value for Pt,  $S(260\text{K}) = -3.8\mu\text{V}/\text{K}$  [38].

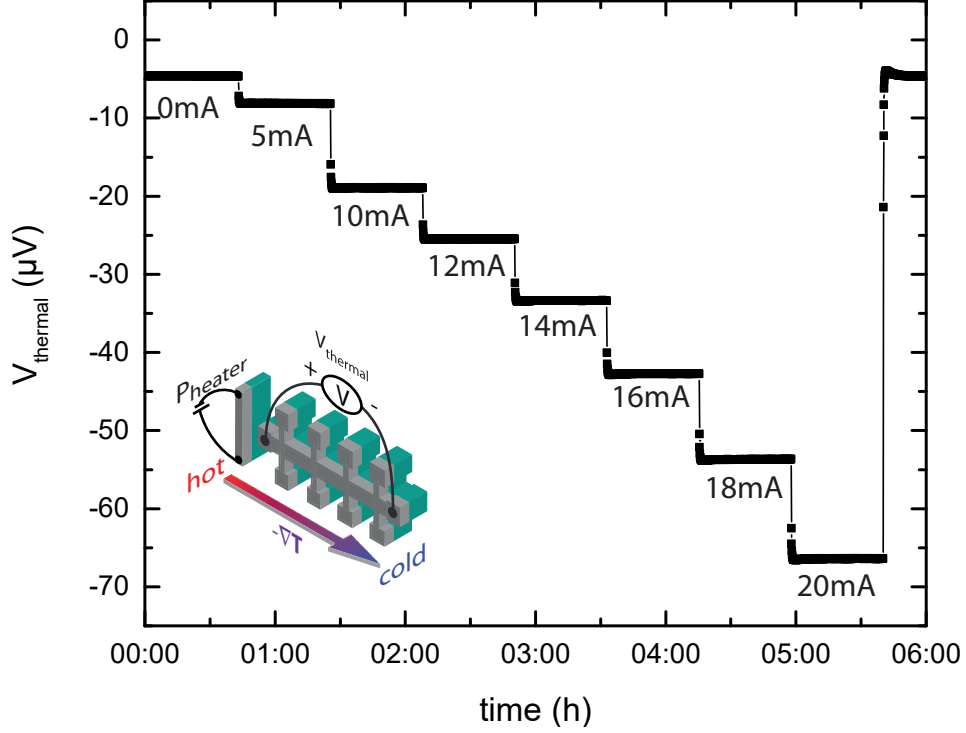


**Figure 7:** Longitudinal thermal voltage  $V_{\text{thermal}}$  taken for a stepwise increase of currents applied to the heater strip. 20 mA correspond to  $P_{\text{heater}} = 286\text{mW}$ .

### Power modulation

To generate large temperature differences along the Hall bar, we use the on-chip heating strip consisting of the same YIG|Pt hybrid structure as the Hall bar. Since the YIG|Pt heterostructure shows spin Hall magnetoresistance (SMR) (i.e., a magnetization-orientation dependent resistance), a modulation of the heating power  $P_{\text{heater}} = R_{\text{heater}} \times I_{\text{heater}}^2$  with magnetization orientation must be taken into account. We measured the magnitude of the SMR effect in our sample to be  $\Delta\rho_1/\rho_0 = (1.0 \pm 0.1) \times 10^{-3}$  at  $T_{\text{base}} = 220\text{K}$  with  $P_{\text{heater}} = 286\text{mW}$  applied to the heating strip. To avoid a SMR-based modulation of the heater

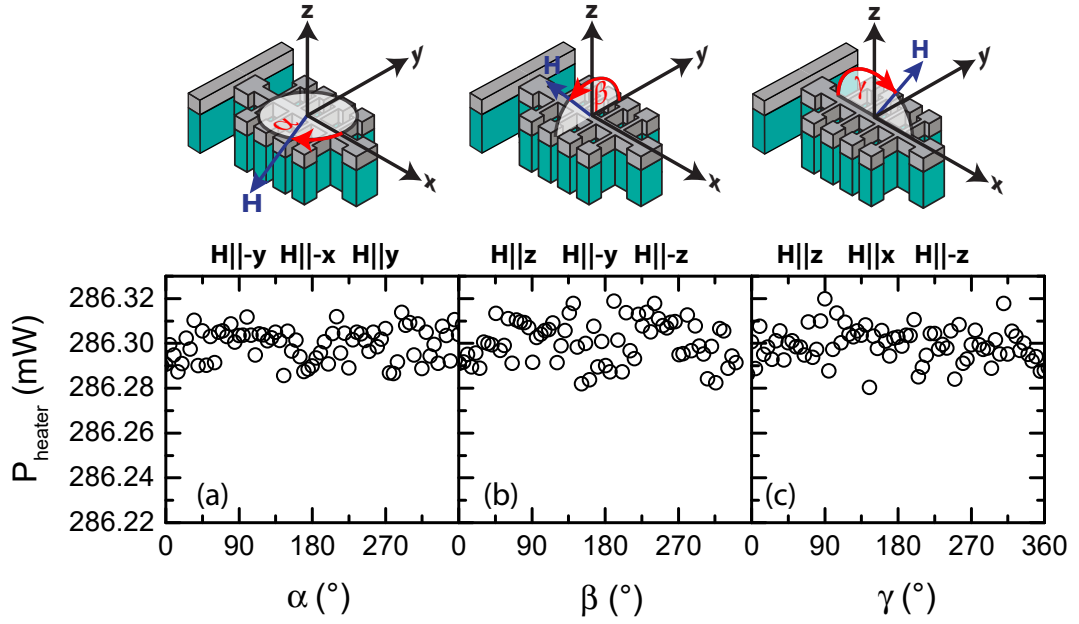


**Figure 8:** Heater power  $P_{\text{heater}}$  as a function of the YIG magnetization orientation in (a) *ip*, (b) *oopx* and (c) *oopy* configuration for  $\mu_0 H = 1$  T. During this measurement, we modulated the current  $I_{\text{heater}}$  applied to the OCH to keep the heating power constant.

power in our magnetization-orientation dependent thermopower measurements, we use a closed-loop control to adjust the applied heater current depending on magnetization orientation, such as to provide a constant heater power of  $P_{\text{heater}} = 286.30$  mW. Using this method, the applied heater power is stabilized with fluctuations smaller than 0.04 mW, see Fig. 8.

#### 8.4 Fingerprint of the SNMTP

For SNMTP experiments, we remove all current sources from the Hall bar ( $I_q = 0$ ) and thermalize the sample to  $T_{\text{base}} = 220$  K. In order to apply a temperature gradient along  $x$  as a driving force, we bias the OCH with the appropriate, magnetization orientation-dependent heater current, such that a constant heater power of  $P_{\text{heater}} = 286$  mW independent of the magnetic field orientation is applied. We rotate a constant external magnetic field  $\mu_0 H = 1$  T around the sample and detect the longitudinal voltage using an Agilent 34420A nanovoltmeter. We use a digital filter to detect the signal and average over 100

power line cycles using the internal filter functions of the nanovoltmeter.

Figure 3 shows the evolution of the longitudinal thermal voltage  $V_{\text{thermal}}$  as a function of the magnetization orientation while rotating an external magnetic field  $\mu_0 H = 1$  T in in-plane (ip,  $(\mathbf{x}, \mathbf{y})$ , panel e), out-of-plane perpendicular  $\mathbf{x}$  (oopx,  $(\mathbf{y}, \mathbf{z})$  plane, panel f) and out-of-plane perpendicular  $\mathbf{y}$  (oopy,  $(\mathbf{x}, \mathbf{z})$  plane, panel g) configuration. For the ip data [cf. Fig. 3(e) in the main text], we find a  $\sin^2 \alpha$  shaped modulation  $\Delta V_{\text{thermal}}$  of about  $-80$  nV on top of the thermopower voltage  $V_{\text{thermal, long}} = -66.225 \mu\text{V}$  given by the Seebeck effect. This modulation is smallest for  $\mathbf{H} \parallel \mathbf{x}$  and  $\mathbf{H} \parallel -\mathbf{x}$ , and largest for  $\mathbf{H} \parallel \mathbf{y}$  and  $\mathbf{H} \parallel -\mathbf{y}$ .

In the oopx rotation geometry [cf. Fig. 3(f)], we find a similar,  $\cos^2 \beta$  shaped modulation on top of the thermopower voltage  $V_{\text{thermal}} = -66.225 \mu\text{V}$  with a modulation amplitude  $\Delta V_{\text{thermal}} \approx 100$  nV slightly increased compared to the ip rotation. Again, a maximum signal is recorded for  $\mathbf{H} \parallel \mathbf{y}$  and  $\mathbf{H} \parallel -\mathbf{y}$  and the level coincides in good approximation with the one detected for the ip rotation. For this oopx geometry, the minima are located at  $\mathbf{H} \parallel \mathbf{z}$  and  $\mathbf{H} \parallel -\mathbf{z}$  and the voltage level for  $\mathbf{H} \parallel \mathbf{z}$  is in good agreement with the signal detected at  $\mathbf{H} \parallel \mathbf{x}$  in ip rotations.

For the oopy rotation [cf. Fig. 3(g)], however, we find no angular dependence of  $V_{\text{thermal}}$  within the noise level of our voltage measurement of 30 nV.

The data set shown in Fig. 3 can be understood in terms of the spin Nernst magneto-thermopower: In our geometry, the temperature gradient along  $\mathbf{x}$  induces a spin Nernst spin current along  $\mathbf{z}$  with spin polarization  $\mathbf{s} \parallel \mathbf{y}$ . Thus,  $\mathbf{H} \parallel \mathbf{y}$  and  $\mathbf{H} \parallel -\mathbf{y}$  correspond to the spin current open circuit boundary condition, since a spin transfer towards the YIG is prohibited for  $\mathbf{H} \parallel \mathbf{s} \parallel \mathbf{y}$ . On the other hand, both  $\mathbf{H} \parallel \pm \mathbf{x}$  and  $\mathbf{H} \parallel \pm \mathbf{z}$  correspond to perfect spin current short-circuit boundary conditions since they allow for a spin transfer. This is in excellent agreement with Eq. (15) discussed in the theory section.

## 8.5 Power and field dependence

On the same sample, we repeated the angle dependent magneto-thermopower measurements for different heating powers between 100 mW and 286 mW resulting in temperature differences between 7.7 K and 18.0 K along the Hall bar as well as for two different magnetic field strengths (0.5 T and 1 T). To extract the modulation amplitudes  $\Delta V_{\text{thermal}}$  and ratios  $\Delta V_{\text{thermal}}/V_{\text{thermal}}$  from our experimental data, we performed  $\cos^2 \delta$  fits.

We observe an increase in the absolute value of the modulation voltage  $\Delta V_{\text{thermal}}$  with increasing  $P_{\text{heater}}$  in ip and oopx rotations. This is shown in Fig. 9(d) and (e) for two different magnetic field magnitudes. For both 0.5 T

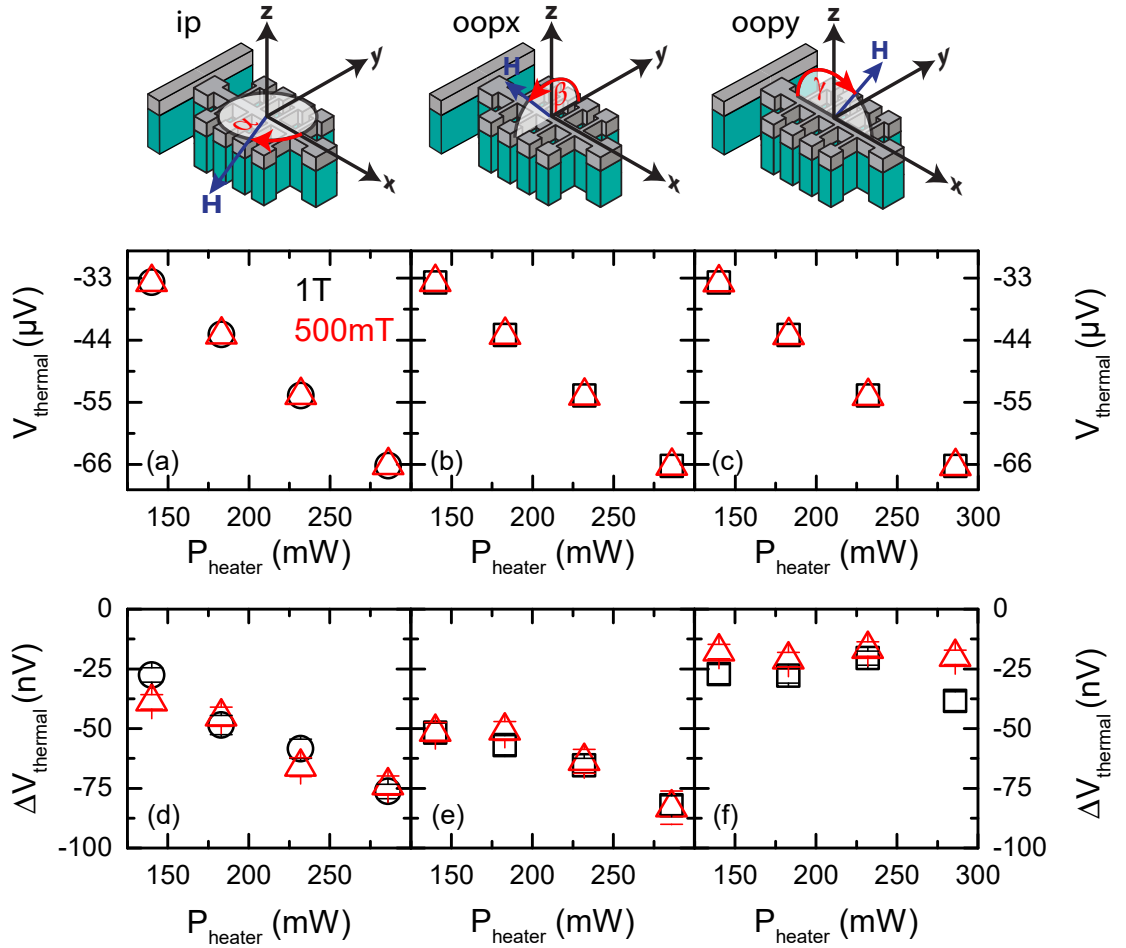


**Figure 9:** (a-c) Power dependence of the thermal voltage  $V_{\text{thermal}}$  and (d-f) the voltage modulation amplitude  $\Delta V_{\text{thermal}}$  for *ip* (left column), *oopx* (middle) and *oopy* rotations (right column) at a base temperature of  $T = 220\text{ K}$  and magnetic field strength of 0.5 T (red triangles) and 1 T (black squares), respectively.

(red triangles) and 1 T (black squares),  $\Delta V_{\text{thermal}}$  increases with increasing  $P_{\text{heater}}$  and the difference between the 0.5 T and 1 T data points is within the experimental error of  $\pm 5$  nV given by the thermal stability of the nanovoltmeters. As the SNMTP can be interpreted as a modulation on the thermal voltage due to a spin current flow across the YIG|Pt interface, the relative amplitude of the modulation of the longitudinal voltage is expected to be independent of both heating power  $P_{\text{heater}}$  and external magnetic field strength  $\mu_0 H$ , as long as a thermally driven spin current is generated. We find that, within the experimental error, the ratio is almost constant as a function of  $P_{\text{heater}}$  and  $\mu_0 H$  for ip and oopx,  $\Delta V_{\text{thermal}}/V_{\text{thermal}} \approx 1.2 \times 10^{-3}$ . For the temperature range studied here (the average sample temperature rises with increasing  $P_{\text{heater}}$ , see Fig. 6),  $\theta_{\text{SH}}$  is known to be almost independent of temperature [26]. Considering  $\Delta V_{\text{thermal}}/V_{\text{thermal}} \approx \text{const.}$ , which is proportional to  $\theta_{\text{SH}}\theta_{\text{SN}}$ , the data in Fig. 9(d) and (e) suggest that the temperature dependence of the spin Nernst angle  $\theta_{\text{SN}}$  is rather weak.

The power dependence of the oopy signal is depicted in Fig. 9(f). As stated by Eq. (15), we expect a constant SNMTP signal as a function of the magnetization orientation in this geometry. While  $\Delta V_{\text{thermal}}$  scales with  $P_{\text{heater}}$  [cf. Fig. 9(d, e)] for ip and oopx rotations, we find that the modulation amplitude observed in oopy is almost constant [ $\Delta V_{\text{thermal}}^{\text{oopy}} \approx -25$  nV, cf. Fig. 9(f)]. Thus, the origin of the modulation in oopy rotations is not related to the spin Nernst magneto-thermopower. However, this power independence can not be explained by the interpretation of  $\Delta V_{\text{thermal}}^{\text{oopy}}$  with a non-vanishing  $\mathbf{y}$  component of  $\nabla T$ . Additionally,  $\Delta V_{\text{thermal}}^{\text{oopy}}$  seems to increase with increasing magnetic field strength. The decrease of  $\Delta V_{\text{thermal}}^{\text{oopy}}(P_{\text{heater}})$  also results in a negative power dependence of the voltage ratio  $\Delta V_{\text{thermal}}^{\text{oopy}}/V_{\text{thermal}}$ . With increasing heater power, the voltage modulation in oopy decreases slightly. This again is at odds with the results found for ip and oopx rotations. In conclusion, due to the absence of a power dependence, the modulation of the thermal voltage in oopy rotations can neither be attributed to the SNMTP concept for  $\nabla T \cdot \mathbf{y} \neq 0$ , nor to parasitic thermopower effects.

## 8.6 Calculation of the spin Nernst angle

Now, we utilize the theory of Sec. 8.1 to extract the heat to spin conversion efficiency for Pt, i.e. the spin Nernst angle  $\theta_{\text{SN}}$ . To this end, we calculate the relative thermopower ratio between open and short-circuit spin current

boundary conditions,

$$\frac{\Delta V_{\text{thermal}}}{V_{\text{thermal}}} = \frac{V_{\text{thermal}}(\mathbf{H} \parallel \mathbf{y}, \text{open}) - V_{\text{thermal}}(\mathbf{H} \perp \mathbf{y}, \text{short})}{V_{\text{thermal}}(\mathbf{H} \parallel \mathbf{y}, \text{open})}. \quad (25)$$

Via Eq. (15), the definitions of  $V_{\text{thermal}}(\mathbf{H} \parallel \mathbf{y}, \text{open})$  and  $V_{\text{thermal}}(\mathbf{H} \perp \mathbf{y}, \text{short})$  read

$$V_{\text{thermal}}(\mathbf{H} \parallel \mathbf{y}, \text{open}) = -(S + \Delta S_0) \Delta T \quad (26)$$

and

$$V_{\text{thermal}}(\mathbf{H} \perp \mathbf{y}, \text{short}) = -(S + \Delta S_0 + \Delta S_1) \Delta T \quad (27)$$

with  $\Delta T = T_{\text{hot}} - T_{\text{cold}} > 0$ . Thus,  $\Delta V_{\text{thermal}}/V_{\text{thermal}}$  corresponds to  $-\Delta S_1/\tilde{S}$  with  $\tilde{S} = S + \Delta S_0$ .

We find  $\Delta V_{\text{thermal}}/V_{\text{thermal}} = -100 \text{ nV}/66.225 \mu\text{V} = -1.5 \times 10^{-3}$  from the raw data taken at 1 T in the oopx plane shown in Fig. 3(f). Based on Eq. (17), we calculate the spin Nernst angle  $\theta_{\text{SN}}$  via

$$\theta_{\text{SN}} \approx -\frac{\Delta S_1}{S} \frac{t_{\text{N}}}{\theta_{\text{SH}} \lambda} \frac{\sigma_{\text{N}} + 2\lambda G_r \coth \frac{t_{\text{N}}}{\lambda}}{2\lambda G_r \tanh^2 \frac{t_{\text{N}}}{2\lambda}}. \quad (28)$$

We use  $G_r = 4.0 \times 10^{14} \Omega^{-1} \text{m}^{-2}$ ,  $\lambda = 1.5 \text{ nm}$  and  $\theta_{\text{SH}} = 0.11$  determined in Ref. [26] for YIG|Pt hybrids at  $T = 250 \text{ K}$  comparable to  $\bar{T} = 255 \text{ K}$  used in our thermopower measurements for this sample. With these parameters, we obtain  $\theta_{\text{SN}} = -0.20$  from Eq. (28).

It seems surprising that we are able to confirm the sign of the spin Nernst angle by transport experiments. Since SMR depends on the square of the spin Hall angle and cannot be used to measure its sign. Similarly, the SNMTP depends on the product of  $\theta_{\text{SN}}$  and  $\theta_{\text{SH}}$ , so from these data alone we cannot conclude that  $\theta_{\text{SN}} < 0$ . We come to our conclusion only because spin pumping measurements conclusively find a positive spin Hall angle in Pt [39]. We note that from a physical point of view  $\theta_{\text{SN}} < 0$  is not problematic at all. In the Sommerfeld approximation it implies that the spin Hall conductivity and its energy derivative at the Fermi energy have opposite signs. Indeed, our first principles calculations of the ratio between  $\theta_{\text{SH}}$  and  $\theta_{\text{SN}}$  find  $\theta_{\text{SH}}/\theta_{\text{SN}} \approx -0.9$  at 250 K [see Sec. 8.2 and Fig. 4(b)]. This beautifully agrees with the ratio  $\theta_{\text{SH}}/\theta_{\text{SN}} \approx -0.5$  found in our experiments.

## References

- [1] Kato, Y. K., Myers, R. C., Gossard, A. C., and Awschalom, D. D. *Science* **306**, 1910–1913 (2004).
- [2] Wunderlich, J., Park, B.-G., Irvine, A. C., Zárbo, L. P., Rozkotová, E., Nemeč, P., Novák, V., Sinova, J., and Jungwirth, T. *Science* **330**, 1801–1804 (2010).
- [3] Sinova, J., Valenzuela, S. O., Wunderlich, J., Back, C. H., and Jungwirth, T. *Review of Modern Physics* **87**, 1213–1260 (2015).
- [4] Valenzuela, S. O. and Tinkham, M. *Nature* **442**, 176–179 (2006).
- [5] Saitoh, E., Ueda, M., Miyajima, H., and Tatara, G. *Applied Physics Letters* **88**, 182509 (2006).
- [6] Uchida, K., Takahashi, S., Harii, K., Ieda, J., Koshibae, W., Ando, K., Maekawa, S., and Saitoh, E. *Nature* **455**, 778 – 781 (2008).
- [7] Jaworski, C. M., Yang, J., Mack, S., Awschalom, D. D., Heremans, J. P., and Myers, R. C. *Nature Materials* **9**, 898–903 (2010).
- [8] Uchida, K., Adachi, H., Ota, T., Nakayama, H., Maekawa, S., and Saitoh, E. *Applied Physics Letters* **97**, 172505 (2010).
- [9] Flipse, J., Bakker, F. L., Slachter, A., Dejene, F. K., and van Wees, B. J. *Nature Nanotechnology* **7**, 166–168 (2012).
- [10] Flipse, J., Dejene, F. K., Wagenaar, D., Bauer, G. E. W., Ben Youssef, J., and van Wees, B. J. *Physical Review Letters* **113**, 027601 (2014).
- [11] Cheng, S., Xing, Y., Sun, Q., and Xie, X. C. *Physical Review B* **78**, 045302 (2008).
- [12] Liu, X. and Xie, X. *Solid State Communications* **150**, 471 – 474 (2010).
- [13] Tauber, K., Gradhand, M., Fedorov, D. V., and Mertig, I. *Physical Review Letters* **109**, 026601 (2012).
- [14] Wimmer, S., Ködderitzsch, D., Chadova, K., and Ebert, H. *Physical Review B* **88**, 201108 (2013).
- [15] Hall, E. *American Journal of Mathematics* **2**, 286 (1879).

- [16] Von Ettingshausen, A. and Nernst, W. *Annalen der Physik und Chemie* **265**, 343 (1886).
- [17] D'akonov, M. I. and Perel, V. I. *JETP Letters* **13**, 467–469 (1971).
- [18] Hirsch, J. E. *Physical Review Letters* **83**, 1834–1837 (1999).
- [19] Betthausen, C., Dollinger, T., Saarikoski, H., Kolkovsky, V., Karczewski, G., Wojtowicz, T., Richter, K., and Weiss, D. *Science* **337**, 324–327 (2012).
- [20] Hoffmann, A. *Magnetics, IEEE Transactions on* **49**, 5172–5193 (2013).
- [21] Ralph, D. C. and Stiles, M. D. *Journal of Magnetism and Magnetic Materials* **320**, 1190 – 1216 (2008).
- [22] Brataas, A., Bauer, G. E., and Kelly, P. J. *Physics Reports* **427**, 157 – 255 (2006).
- [23] Nakayama, H., Althammer, M., Chen, Y.-T., Uchida, K., Kajiwara, Y., Kikuchi, D., Ohtani, T., Geprägs, S., Opel, M., Takahashi, S., Gross, R., Bauer, G. E. W., Goennenwein, S. T. B., and Saitoh, E. *Physical Review Letters* **110**, 206601 (2013).
- [24] Vlietstra, N., Shan, J., Castel, V., Ben Youssef, J., Bauer, G. E. W., and van Wees, B. J. *Applied Physics Letters* **103**, 032401 (2013).
- [25] Althammer, M., Meyer, S., Nakayama, H., Schreier, M., Altmannshofer, S., Weiler, M., Huebl, H., Geprägs, S., Opel, M., Gross, R., Meier, D., Klewe, C., Kuschel, T., Schmalhorst, J.-M., Reiss, G., Shen, L., Gupta, A., Chen, Y.-T., Bauer, G. E. W., Saitoh, E., and Goennenwein, S. T. B. *Physical Review B* **87**, 224401 (2013).
- [26] Meyer, S., Althammer, M., Geprägs, S., Opel, M., Gross, R., and Goennenwein, S. T. B. *Applied Physics Letters* **104**, 242411 (2014).
- [27] Chen, Y.-T., Takahashi, S., Nakayama, H., Althammer, M., Goennenwein, S. T. B., Saitoh, E., and Bauer, G. E. W. *Physical Review B* **87**, 144411 (2013).
- [28] Takahashi, S., Imamura, H., and Maekawa, S. In *Concepts in Spin electronics*, Maekawa, S., editor, 343–370. Oxford University Press, New York (2006).
- [29] Jia, X., Liu, K., Xia, K., and Bauer, G. E. W. *Europhysics Letters* **96**, 17005 (2011).

- [30] Valet, T. and Fert, A. *Physical Review B* **48**, 7099–7113 (1993).
- [31] Vernes, A., Györffy, B. L., and Weinberger, P. *Physical Review B* **76**, 012408 (2007).
- [32] Lowitzer, S., Gradhand, M., Ködderitzsch, D., Fedorov, D. V., Mertig, I., and Ebert, H. *Physical Review Letters* **106**, 056601 (2011).
- [33] Butler, W. H. *Physical Review B* **31**, 3260–3277 (1985).
- [34] Banhart, J., Bernstein, R., Voitländer, J., and Weinberger, P. *Solid State Communications* **77**, 107 – 110 (1991).
- [35] Lowitzer, S., Ködderitzsch, D., and Ebert, H. *Physical Review Letters* **105**, 266604 (2010).
- [36] Jonson, M. and Mahan, G. D. *Physical Review B* **21**, 4223–4229 (1980).
- [37] Geprägs, S., Meyer, S., Altmannshofer, S., Opel, M., Wilhelm, F., Rogalev, A., Gross, R., and Goennenwein, S. T. B. *Applied Physics Letters* **101**, 262407 (2012).
- [38] Moore, J. P. and Graves, R. S. *Journal of Applied Physics* **44**, 1174–1178 (1973).
- [39] Czeschka, F. D., Dreher, L., Brandt, M. S., Weiler, M., Althammer, M., Imort, I.-M., Reiss, G., Thomas, A., Schoch, W., Limmer, W., Huebl, H., Gross, R., and Goennenwein, S. T. B. *Physical Review Letters* **107**, 046601 (2011).